JGR Space Physics

RESEARCH ARTICLE
10.1029/2022JA030568

**Key Points:**

- Coronal Mass Ejection (CME) storms produce more enhancements down to the lower *L*-values for $O^+$, $He^+$, and $H^+$ ions at ≤50 keV energies
- For $L = 2–5.5$, ≥1 keV $O^+$, $He^+$, and $H^+$ ion fluxes show highest correlation with −Sym-H during CME storms
- During CIR storms, $O^+$, $He^+$, and $H^+$ ion fluxes remain at high for a longer period of time than during CME storms

**Correspondence to:**

M. Pandya,
pandya.meghamahendra.3j@kyoto-u.ac.jp

**Citation:**

Pandya, M., Bhaskara, V., Ebihara, Y., & Reeves, G. D. (2022). *L*-value and energy dependence of 0.1–50 keV $O^+$, $He^+$, and $H^+$ ions for CME and CIR storms over the entire Van Allen Probes era. *Journal of Geophysical Research: Space Physics*, *127*, e2022JA030568. https://doi.org/10.1029/2022JA030568

Received 18 APR 2022
Accepted 11 SEP 2022



# *L*-Value and Energy Dependence of 0.1–50 keV $O^+$, $He^+$, and $H^+$ Ions for CME and CIR Storms Over the Entire Van Allen Probes Era

**Megha Pandya[1,2], Veenadhari Bhaskara[2], Yusuke Ebihara[1], and G. D. Reeves[3]**

[1]Research Institute for Sustainable Humanosphere, Kyoto University, Uji, Japan, [2]Indian Institute of Geomagnetism, Navi Mumbai, India, [3]Intelligence and Space Research Division, Los Alamos National Laboratory, Los Alamos, NM, USA

**Abstract** Our studies report the first observation of *L*-value and energy sorted correlation of differential fluxes of 0.1–50 keV $O^+$, $He^+$, and $H^+$ ions with different geophysical parameters for 29 Coronal Mass Ejected (CME) and 40 Corotating Interaction Region (CIR)-driven geomagnetic storms during the entire Van Allen Probes era. For both solar wind drivers, ions with ≥1 keV energies show more variability in response to the solar wind changes, while the lower energy (<1 keV) ions are relatively stable. During the in-storm interval, $O^+$ ions show maximum flux enhancement and become further prominent during CME storms. $O^+$ ion (≥10 keV) fluxes show good correlation with $-V_{sw}B_z$, and Sym-H index during CME-driven storms in the $L \sim 2.5–5.5$. Apart from this, the average duration of persistence ($\langle \Delta t \rangle$) for enhanced fluxes is higher for CIR-driven storms with $\langle \Delta t \rangle_{O^+} > \langle \Delta t \rangle_{He^+} > \langle \Delta t \rangle_{H^+}$ at $E \leq 50$ keV in the $L \sim 2.5–5.5$. Moreover, the observed value of $\langle \Delta t \rangle_i$ (where *i* is $O^+$, $H^+$ or $He^+$) increases with the increasing *L*. We discuss the plausible mechanisms to provide a comprehensive overview of *L*-values and energy sorted $O^+$, $He^+$ and $H^+$ ion dynamics for two different categories of solar wind drivers.

**Plain Language Summary** $O^+$, $He^+$, and $H^+$ ions having energies ranging from ∼10 eV to 50 keV contribute to a majority of the ring current density that provides significant information about the important processes in the inner magnetosphere. In this study, we acquire high-resolution data over the entire Van Allen Probes era to understand storm time dynamics of ion fluxes for the two different categories of solar wind drivers. We find a characteristic difference upon correlating the ion flux enhancement during the storm main phase with the solar wind parameters and strength of the magnetic storm at different *L*-values and energies for both the category of solar wind drivers. Not all the energies and *L*-values respond in a similar manner. Moreover, $O^+$, $He^+$, and $H^+$ do not appear at the spacecraft location for the same duration of time. The time duration for which the ion fluxes remain at high is more for Corotating Interaction Region (CIR)-driven storms than Coronal Mass Ejected (CME) ones. Our studies give a comprehensive overview of spatio-temporal characteristics of the inner magnetospheric $O^+$, $He^+$, and $H^+$ ions at different energies using a long-term data set for CME and CIR-driven geomagnetic storms.

## 1. Introduction

The variation of energetic ion composition in the ring current during geomagnetically disturbed intervals has been extensively studied in various aspects since the 1980s. The ring current primarily comprises of ∼1–200 keV ions (mainly $O^+$, $He^+$, and $H^+$) and electrons in the region of ∼2–7 $R_E$ (Daglis et al., 1999; Gonzalez et al., 1994; Hamilton et al., 1988). The energy density of $O^+$ ions is usually comparable to the $H^+$ ions and sometimes dominates the $H^+$ ions during the geomagnetic storms (Daglis et al., 1998; Gloeckler et al., 1985; Hamilton et al., 1988). Earth's plasma sheet is the main region for transporting ions from solar wind and ionospheric origin to the inner magnetosphere, where $O^+$ and $He^+$ ions increase in comparison with that of $H^+$ ions (Nosé et al., 2001).

The structure and dynamics of the ring current are determined by these particle populations, which are largely controlled by the time-varying magnetic and electric fields depending on solar wind conditions. Mainly, two types of solar wind drivers are responsible for magnetic storms, that is, Coronal Mass Ejection (CME) and Corotating Interaction Region (CIR) (Borovsky & Denton, 2006; Gonzalez et al., 1999).

The response of the ring current ion composition is very different for both the geomagnetic solar wind drivers (Cramer et al., 2013; Katus et al., 2015; Liemohn & Katus, 2012; Mouikis et al., 2019). As compared with CME-driven storms, the CIR-driven storms show the larger energy deposit in the inner magnetosphere than the input energy (Turner et al., 2009), which can be attributed to the characteristic difference in the solar wind driving conditions during CME and CIR events.

The immediate cause for the buildup of ring current is the accumulation of hot plasmas, in particular ions that are primarily transported by the magnetospheric convection associated with the reconnection of IMF with Earth's magnetic field (Ebihara & Ejiri, 2003 and references therein). In that sense, the ring current is thought to be built well when the magnetospheric convection is strong, and the plasma sheet density is high (Ebihara & Ejiri, 2000; Kozyra, Fok, et al., 1998; Thomsen et al., 1998). The strength of the convection depends on the solar wind velocity ($V_{sw}$) and the southward component of the interplanetary magnetic field (IMF) (e.g., Boyle et al., 1997; Siscoe, 2002; Weimer, 2001). The enhancement of the convection gives rise to an earthward adiabatic transport of the nightside plasma sheet ions deep into the inner magnetosphere (A. J. Chen, 1970), leading to the ring current development (M. W. Chen et al., 1998; Ebihara & Ejiri, 2000; Fok et al., 2001; Jordanova et al., 1998; Kistler et al., 1989; Lee et al., 1983; Takahashi et al., 1990). Indeed, the Dst variations during the storm main and recovery phases are well reproduced by an empirical model depending on $V_{sw}$ and the southward component of IMF (Burton et al., 1975).

In the keV-range, $H^+$, $He^+$, $He^{++}$, $O^+$, $O^{++}$, $O^{\geq+3}$, and $C^{6+}$ ions are known to coexist in the inner magnetosphere, implying that the ions originate in the solar wind and the ionosphere (Allen et al., 2016; Ebihara et al., 2009; Fennell et al., 1996; Gloeckler et al., 1985; Kremser et al., 1987; Krimigis et al., 1985). For the ions originating in the solar wind (Kremser et al., 1987), the plasma sheet density ($N_{ps}$) is known to be correlated with the solar wind density ($N_{sw}$) (Borovsky et al., 1998; Ebihara & Ejiri, 2000; Terasawa et al., 1997) although the entry process is not well known. Nosé et al. (2005) correlated the number density of 9–135 keV $O^+$, $He^+$, and $H^+$ ions in the plasma sheet with the solar wind number density. They found that the plasma sheet $H^+$ ion number density shows good correlation with $N_{sw}$, while the $O^+$ and $He^+$ number density had no correlation with the $N_{sw}$. High-charge state oxygen ions, which are believed to be the solar wind origin, are observed to increase in the inner magnetosphere during magnetic storms (Allen et al., 2016; Ebihara et al., 2009). For the ions originating from the ionosphere, numerous studies have demonstrated that $O^+/H^+$ ratio of ion flux increases as the strength of geomagnetic activity increases (e.g., Kistler et al., 1989; Kronberg et al., 2012; Lundin et al., 1980; Nose et al., 2005; Roeder et al., 1996). Kronberg et al. (2012) performed a statistical study of ions having energies ≥275 keV, and showed that higher $O^+/H^+$ intensity ratio for lower AE-index (200–300 nT) and its standard deviation gradually increased with increasing AE-index. The $O^+$ number density in the plasma sheet is well correlated with the solar wind kinetic energy flux, which is the product of solar wind dynamic pressure ($P_{dy}$) and $V_{sw}$ (Lennartsson, 1995). Moore et al. (2001), Moore et al. (1999), and Elliott et al. (2001) have shown that ionospheric plasma outflow responds to the $P_{dy}$ which can be a source of the ions in the near-Earth plasma sheet. Elliott et al. (2001) also found a good correlation between the density of outflowing $O^+$ and $P_{dy}$. Kronberg et al. (2014) showed that the $O^+$ ions are best correlated with $P_{dy}$ and the *z*-component of the IMF $B_z$. Most of the previous studies have used integrated values, such as number density, energy density, plasma pressure, and flux integrated over energy to demonstrate the response of energetic ion composition in the Earth's inner magnetosphere to disturbed conditions. Energy and *L* dependence of the energetic ion composition on the solar wind and the magnetospheric conditions are not well known.

The decay of these energetic particle population developed in the Earth's inner magnetosphere occurs due to loss mechanisms like, charge exchange (e.g., Dessler & Parker, 1959; Ebihara & Ejiri, 2003; Kistler et al., 1989), Coulomb collision (e.g., Fok et al., 1991, 1993), wave-particle interaction (e.g., Jordanova et al., 2001; Usanova et al., 2010). In addition to the charge exchange and Coulomb collision (e.g., Daglis et al., 1999; Fok et al., 1991, 1993), the precipitation loss (Kozyra, Jordanova, et al., 1998; Walt & Voss, 2001) and ion escape through the magnetopause (Keika et al., 2005; Zong et al., 2001) also acts as a major mechanism for the loss of $O^+$, $He^+$, and $H^+$ ions in the ring current region. The different times for buildup and disappearance of each ion species in this energy range (10–500 eV) can be explained by showing the difference in their decay lifetimes.

In the present studies, we provide an understanding of the impact of both the solar wind drivers on $O^+$, $He^+$, and $H^+$ at different energies, *L*-values and storm phases of statistically significant number of geomagnetic storms that occurred over the entire Van Allen Probes era. The energy and *L*-value sorted correlation of $O^+$, $He^+$, and $H^+$ ion differential flux with various geophysical parameters for both the solar wind drivers is reported for the first time. We also compare the average duration of persistence ($\langle \Delta t \rangle_i$, where $i$ is the ion species) of $O^+$, $He^+$, and $H^+$ ions during storm recovery phase for CME and CIR-driven storms by using the observations from Van Allen Probes that cover a wide range of energy and $L$-values.

## 2. Data and Methodology

We used omnidirectional-averaged fluxes of $O^+$, $He^+$, and $H^+$ over the entire Van Allen Probes era (i.e., from October 2012 to 2019), and characterized their dependence on the geomagnetic activity. The solar wind parameters and 1-min resolution symmetric component of ring current (Sym-H) are taken from OMNI data set. We selected the geomagnetic storms with minimum Sym-H being less than −50 nT, and divided them, in terms of the driver, namely, CME and CIR. The list of CME and CIR-driven magnetic storms is verified by Pandya et al. (2019) and CCMC Space Weather Database Of Notifications, Knowledge, Information (DONKI) database. This paper closely follows the data selection and methodology described in Pandya et al. (2019) but for keV ions. The ion fluxes taken from Helium, Oxygen, Proton, and Electron (HOPE) instrument (Funsten et al., 2013) on-board NASA's Van Allen Probes mission were used. For each magnetic storm, the ion fluxes are separated during each inbound and outbound passages of Van Allen Probes-A and B orbit and averaged over each storm phase. For identifying each storm phase, we follow the procedure as shown in Pandya et al. (2019). They defined “at-storm” interval as the duration from the time the *Dst* index begins to decrease after sudden commencement until the *Dst* minimum. “Pre-storm” interval is defined as the interval 1–3 days before the sudden commencement, while the “post-storm” interval is defined as the duration 1–5 days after the *Dst*-minimum. We replace the word “at-storm” defined by Pandya et al. (2019) with “in-storm” keeping the methodology same for the identification of the in-storm interval. Thus, in-storm interval includes only the main phase of the storm. Hence, we have two observations of ion fluxes at a given $L$-value and energy during each orbit of the Van Allen Probes A and B.

Here, we emphasize that the $L$-value used in this study is Roederer's $L$-parameter ($L^*$) (Roederer, 1970). It is given by the following equation:

$$L^* = \frac{2\pi k_0}{\Phi R_E} \tag{1}$$

where $k_o$ is the dipole moment, Φ is the magnetic flux enclosed by ion's drift contour.

Since, the ion's drift contour depends on the magnetic field configuration, the OP77Q external field model (Olson & Pfitzer, 1979) and IGRF internal field model (Finlay et al., 2010) have been obtained from the LANLGeoMag library and invoked in the calculation of $L^*$. During a geomagnetic storm, the azimuthal asymmetry in the magnetospheric magnetic field increases and attains a non-dipolar like configuration (Koskinen & Kilpua, 2022). When the guiding center of a stably trapped ion drifts around the Earth in a non-dipolar magnetic field configuration, it traces a drift shell which is asymmetric around the dipole axis. Hence, it is valid to utilize Roederer's $L$-value while comparing the ion fluxes between different storm phases.

The Van Allen Probes mission consists of two identically instrumented spacecraft (probes A and B) that were launched into near-equatorial orbit (10° inclination) with the orbital period of ∼9 hr, a perigee at ∼1.1 $R_E$, and an apogee at ∼5.8 $R_E$ (Mauk et al., 2012). Here, we perform the statistical analysis by using level-2 spin-averaged measurements obtained at nearly every 24 s with 72 logarithmically spaced energy channels ranging from 1 eV to 50 keV (Funsten et al., 2013).

For the better identification of maximum flux variations, we calculate $j_{\max}(L, K)$, which is the maximum value of the spin-averaged differential flux over a specified storm phase at a given $L$-value and kinetic energy $K$.

The $O^+$, $He^+$, and $H^+$ ion fluxes are averaged over bins in $L$-values with bin-width 0.05 and at every 0.25 $L$-value. The HOPE energies are logarithmically spaced and are shifted upwards during its passage on perigee; hence, we cannot directly consider all the available energies in the HOPE instrument for long-term studies. To easily represent and understand the impact of different solar wind drivers on the variability of ions that belongs to the different plasma populations, we restrict our studies to the selected seven bands of kinetic energies ($K$), namely 0.1, 1, 10, 20, 30, 40, and 50 keV. The energy bin width is <±5% of each measured energy. Following Reeves et al. (2003), Temporin and Ebihara (2011), and Pandya et al. (2019), we employ the change in fluxes with a

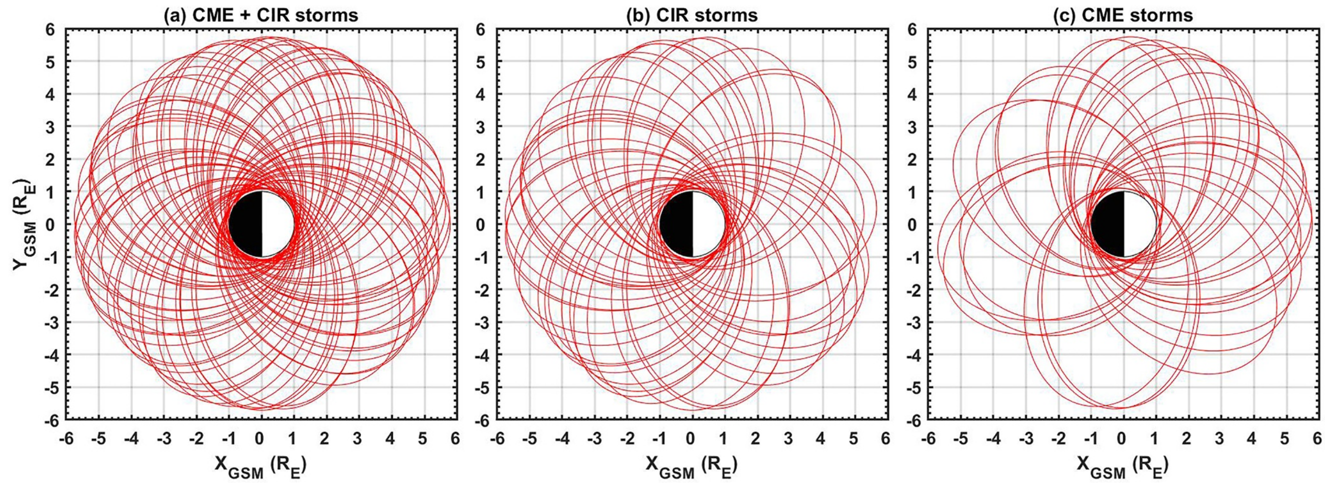


**Figure 1.** Trajectories of the Van Allen Probes-A in the X-Y plane during (a) CME and CIR storms, (b) CIR storms, and (c) CME storms.

factor of 2, at a particular energy and $L$-value, for the pre-, in-, and post-storm characterization of enhancement, depletion, or no-change. During the main phase of the storm, overall ring current enhances and hence the population of keV ions rises up for most of the events. Hence, we focus only on the enhancement events for our studies. We calculate the ratio of flux taken during the storm interval ("in-storm") to that taken during the pre-storm interval ("pre-storm") as,

$$R_1(L,K) = \frac{j_{\max}(L,K)|_{in-storm}}{j_{\max}(L,K)|_{pre-storm}} \tag{2}$$

For most of the events, $R_1(L, K)$ continuous to remain at high ($\geq$2) and does not cease so easily just after the main phase of the geomagnetic storm has passed. Sometimes $R_1(L, K) \geq 2$ for an extended period in the early recovery phase. The early recovery phase is considered to cease when 60% of the minimum Sym-H is recovered for a given geomagnetic storm. Hence, the ratio of fluxes from the main phase and early recovery phase of the storm interval to the pre-storm interval is calculated as:

$$R_2(L,K) = \frac{j_{\max}(L,K)|_{in-storm\ and\ early\ recovery\ phase\ of\ the\ storm}}{j_{\max}(L,K)|_{pre-storm}} \tag{3}$$

We define the enhancement of fluxes when the absolute value of ratio (i.e., $R_1$ or $R_2$) increases by a factor of 2 or above. The distribution of ion fluxes is not axisymmetric with respect to the Earth's dipole moment. Thus, we compile a robust data set of 40 CIR-driven and 29 CME-driven geomagnetic storms sorted according to its inbound/outbound passage, energies, $L$-value and phases of the geomagnetic storm that occurred during the entire Van Allen Probes era. Figure 1 gives the passages of Van Allen probes-A spacecraft for the (a) CME and CIR geomagnetic storms, (b) 40 CIR-driven, and (c) 29 CME-driven geomagnetic storms.

## 3. Observation and Analysis

Figure 2 summarizes the statistical distribution of enhancement events across the different energies and $L$-value. Left half of Figure 2 shows the percentage of total flux enhancement events during CIR-driven storms, while the right half corresponds to the CME-driven storms as a function of $L$-value and energy. Panels a1-a2, b1–b2, and c1–c2 show the percentage of total events with $R_1 \geq 2$ for $O^+$, $He^+$, and $H^+$ ions, respectively. The open boxes indicate the total number of events being <3 at a given energy and $L$-value, which are excluded from our analysis.

The distribution of percentage of events with $R_1 \geq 2$ is very similar for CME and CIR-driven geomagnetic storms. However, the percentage number of the CME-driven geomagnetic storms is higher down to the lower $L$-values for all the energies and ion species. Also, there are relatively higher percentage of $O^+$ ion enhancement events (panels (a1–a2)) than $He^+$ and $H^+$ in the $L$ ~3.5–5.5 for ≥20 keV. These observations in Figure 2 are consistent

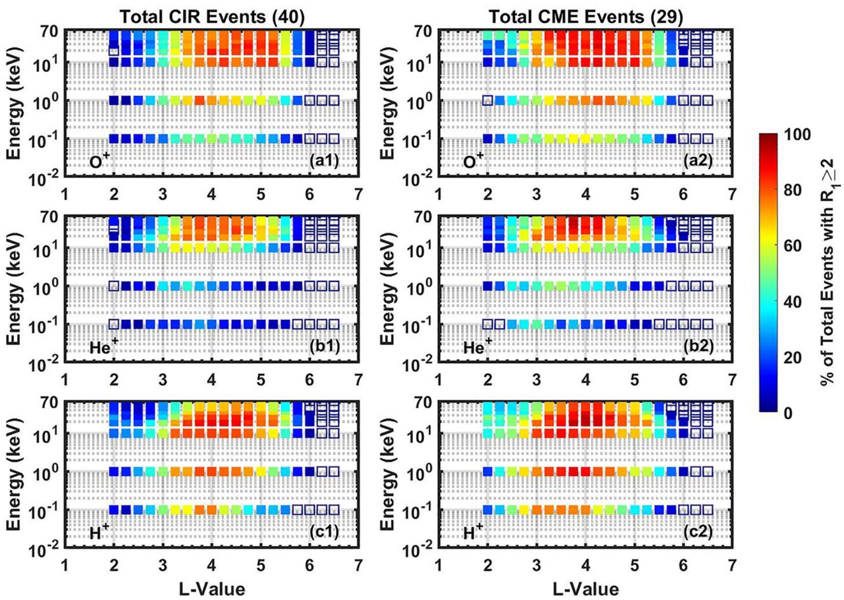


**Figure 2.** Statistical distribution of $R_1 \geq 2$ occurrences. The CIR-driven storms are shown on the left half, while CME-driven storms are on the right. Each panel shows the percentage of all events in color that result in an enhancement of $O^+$ (a1–a2), $He^+$ (b1–b2), and $H^+$ (c1–c2) ions as a function of $L$-value and ion energy.

with the previous studies by several researchers like Daglis et al. (1998), Gloeckler et al. (1985), and Hamilton et al. (1988), where they showed events with higher $O^+$ ion flux than $He^+$ and $H^+$ with energy higher than 50 keV.

### 3.1. Estimation of Ion Flux Enhancement

Figure 3 provides the quantitative examination of the nature of $O^+$, $He^+$ and $H^+$ ion flux variability across different energies and $L$-values. $\bar{R}_1(L, K)$ is the averaged value of $R_1(L, K)$, which is a ratio of flux taken in the "in-storm" time to that in "pre-storm" time.

The two columns from the left end show $\bar{R}_1(L, K)$ for $O^+$ (a1–a2), $He^+$ (b1–b2), and $H^+$ (c1–c2) ions as a function of $L$-value and ion energy for CIR (a1–b1–c1) and CME (a2–b2–c2) driven storms. Color indicates $\bar{R}_1(L, K)$. The size of each diamond represents the percentage of all events with $R_1 \geq 2$ (shown by color in Figure 1). The $y$-axis is broken so as to shrink the empty space between 1 and 10 keV and enhance the readability for the smaller segments of 0.1 and 1 keV. The two columns from the right end show its significance in statistical terms. To evaluate the significance of $\bar{R}_1(L, K)$ we calculate two important statistical parameters. The first is the interquartile range ($IQR$) of the distribution.

It gives the measure of spread that is obtained by calculating the range of the middle 50% of scores in an ordered set of data (Clark-Carter, 2005). In other words, the difference between the upper quartile ($Q3$) and the lower quartile ($Q1$) gives the $IQR$. It is calculated as

$$IQR = Q3 - Q1 \tag{4}$$

where,

$$Q1 = \frac{n+1}{4}\text{term} \tag{5}$$

$$Q3 = \frac{3(n+1)}{4}\text{term} \tag{6}$$

Here, $n$ is the total number of data points falling into a bin. Thus, $Q1$ (or $Q3$) represents the value under which 25% (or 75%) of data points are found when they are arranged in increasing order. The second important statistical quantity is skewness ($Sk$) of the distribution. It is calculated as follows:

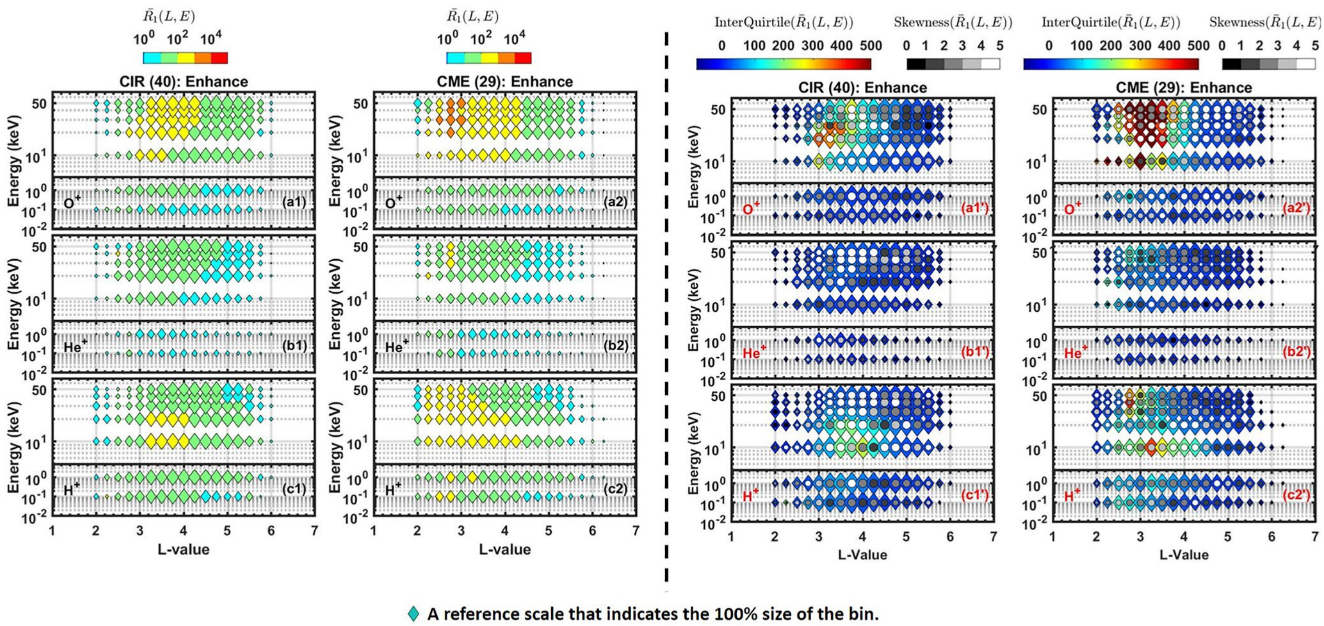


**Figure 3.** The black dashed vertical line separates $\bar{R}_1(L,K)$ $(left)$ from its significance in statistical terms (right). The $\bar{R}_1(L,K)$ for $O^+$ (a1–a2), $He^+$ (b1–b2), and $H^+$ (c1–c2) ion as a function of $L$-value and ion energy for CIR (a1–b1–c1) and CME (a2–b2–c2) driven storms is shown. Color on the left half gives $\bar{R}_1(L,K)$. The percentage of all events with $R_1 \geq 2$ is represented by the size of each diamond (same as colorbar in Figure 1). A reference bin scale at 100% size is shown at the bottom of the figure. The $y$-axis is broken and adjusted such that it covers all the bands of selected energies. The right half of the panel representation is same as left half, except for the colorbar. Color gives the interquartile range of $\bar{R}_1(L,K)$, while gray-color scale gives the skewness of the distribution.

$$Sk = \frac{\frac{1}{n}\sum_{i=1}^{n}(x_i - \mu)^3}{\sigma^3} \tag{7}$$

where $n$ is the number of data points falling into a bin, $x_i$ is the $i$th observation, $\mu$ is the mean of all the observations, and $\sigma$ is the standard deviation. Skewness describes the amount by which a distribution deviates from Gaussian distribution. There are equal number of measurements above and below the mean in a Gaussian distribution with the same value of mean, median, and mode. For such a distribution, the skewness is 0. If the values of mean, median, and mode are not same, then the distribution is more stretched out on the either side and the distribution may be skewed. If the peak of the distribution is shifted on the right side from a normal distribution then it is called negatively skewed, while the distribution is said to be positively skewed if its peak is shifted to the left side from a normal distribution. Two columns on the right end of Figure 3 give the $IQR$ and $Sk$ for the CIR and CME storms. The color scale gives the $IQR$ of $\bar{R}_1(L,K)$, while the gray-color scale gives $Sk$ of the distribution.

Panels a1–a2 show that the $\bar{R}_1(L,K)$ is similar for $O^+$ ions regardless of the solar wind driver. However, at $L \leq 3$, $E \geq 20$ keV $\bar{R}_1(L,K)$ for CME is higher than CIR. To test the reliability of $\bar{R}_1(L,K)$ we utilize statistical methods like $IQR$ and $Sk$ shown on the right half of Figure 3. Panels a1′–a2′ show a significant difference in the $IQR$ (indicated by color) for $L$ ~2.5–4 at ≥1 keV. Here, $IQR$ for CME storms is much larger than CIR storms indicating higher contribution in $\bar{R}_1(L,K)$ from the extreme values during CME storms. As skewness of the distribution is positive (gray-scale), the extreme values indicate the fluxes observed on the higher end. Moreover, we have calculated an additional statistical property of the distribution called kurtosis, which describes the measure of peakedness of a distribution (Chissom, 1970). Kurtosis is calculated as:

$$k = \frac{\Sigma(x-\mu)^4}{n\sigma^4} \tag{8}$$

The value of $k$ represents whether the data are heavy-tailed or light-tailed relative to a Gaussian distribution. For a Gaussian distribution, the value of $k$ turns out to be 3. For our studies, we found that kurtosis is >3 for the entire analysis (not shown). Hence, the distribution in our analysis is heavy-tailed and we can say that $O^+$ ion fluxes have enhanced to a greater value for CME-driven storms than CIR-ones for $L$ ~2.5–4.25 at ≥1 keV. For $L \geq 4.25$ at ≥1 keV $\bar{R}_1(L, K)$ is nearly in the same range (panels a1–a2) and $IQR$ is also nearly same, but $Sk <$ ~2 in a1′, while $Sk$ ~3–4 in a2′. So, CIR-driven storms have more symmetric distribution around $\bar{R}_1(L, K)$ than CME storms, while there exists very few events with extreme fluxes in CME-driven storms. The lower energy (<1 keV) $O^+$ $\bar{R}_1(L, K)$ (a1–a2) does not vary a lot with $L$-values or solar wind drivers. Also, $O^+$ ion enhancement is maximum in panel a2 than in any other panels (a1, b1–c2) in Figure 3. This indicates that the $O^+$ ion shows maximum increase during CME storms panels b1–b2 show that an overall distribution of $\bar{R}_1(L, K)$ is nearly same for CME and CIR storms but a slight increase in $\bar{R}_1(L, K)$ is observed at $L = 2.75$–3. Though, the distribution of enhanced $He^+$ ion fluxes looks the same for CME and CIR-driven storms (b1–b2), increased fluxes with higher $IQR$ and more symmetric distributions ($Sk$) are observed for CME-driven storms (panels b1′–b2′).

Similarly, in panels c1–c2, we find that $\bar{R}_1(L, K)$ for $H^+$ has enhanced to a greater amount for CME-driven storms (c2) than CIR-ones (c1) for $L$ ~2–3 at ≥30 keV with the $L$-values extending up to 3.5. The $H^+$ ion fluxes with energies 1–10 keV also enhance for $L \leq 4$. In both the energy bands, panel c2′ indicates that there exists more symmetric distribution ($Sk$) about extreme values ($IQR$) than panel c1′, indicating that the $H^+$ ion fluxes are more enhanced for CME-driven storms than CIR-ones. Comparing the overall picture, panels c1–c2 show that $\bar{R}_1(L, K)$ is greater for $H^+$ ions than corresponding $He^+$ ions band (b1–b2). Nevertheless, $O^+$ ion fluxes (a1–a2) show the highest $\bar{R}_1(L, K)$. For >1 keV $O^+$, $He^+$, and $H^+$ ions at $L > 4$, the $\bar{R}_1(L, K)$, $Sk$ and $IQR$ show not much difference for CME and CIR storms, indicating similar behavior of all the ion flux increase for CME and CIR storms. This is the same case across all the $L$-values having energies <1 keV.

### 3.2. Relationship of Ion Fluxes With Various Geophysical Parameters

To investigate the dependence of various parameters on the inner magnetospheric ions, we present Figure 4. It gives the correlation between $O^+$, $He^+$, and $H^+$ ion fluxes with $V_{sw}$ times −IMF $B_z$ (panels a1–a2–a3, a1′–a2′–a3′), $P_{sw}$ (panels b1–b2–b3, b1′–b2′–b3′), $N_{sw}$ (panels c1–c2–c3, c1′–c2′–c3′), − Sym-H (panels d1–d2–d3, d1′–d2′–d3′) and AE-index (panels e1–e2–e3, e1′–e2′–e3′) as a function of energy and $L$-value. Here, we calculate linear correlation coefficients (CC) between various parameters and the logarithm of ion fluxes. To avoid the inaccuracy in our statistics, bins with number of data points <3 are shown in the open boxes. Black-dashed horizontal line separates the CIR-driven storms (upper half) from the CME-driven storms (lower half). The range of the color bar is same for solar wind parameters and geomagnetic index for both the category of solar wind drivers.

For CME storms, the $-V_{sw}B_z$ has high correlation with ion fluxes over $L$ ~2.5–5 and ≥10 keV with CC of $O^+$ ion fluxes being greater than $He^+$ ion fluxes which is, in turn, greater than $H^+$ ion fluxes (panels a1′–a2′–a3′), while CIR storms have relatively lower CC with $-V_{sw}B_z$ (panels a1–a2–a3). In panel b1′, $O^+$ ion flux and $P_{sw}$ show a high correlation over much wider energy and $L$-value, while for $He^+$, $H^+$ ion fluxes, a fairly good correlation with $P_{sw}$ is observed over restricted energies and $L$-value (panels b2′–b3′). $N_{sw}$ is observed to show poor correlation with fluxes of $O^+$ ions for any $L$-value and energy band for both CME and CIR-driven storms (c1–c1′), while CC of ~0.5 is observed for $He^+$and $H^+$ ion fluxes for both the solar wind drivers (c2–c3, c2′–c3′). Comparing panels d1–d2–d3 with d1′–d2′–d3′, we find that $O^+$, $He^+$, and $H^+$ ion fluxes have greater correlation with − Sym-H index for CME-driven storm than CIR ones covering the entire band of $L$-values and energies > ~1 keV. Though CIR-driven storms show greater correlation in d1–d2–d3 but it is limited to a spatial extent <3.5, while for CME storms, the enhancement is observed across all the $L$-values. The AE-index shows a greater correlation with the fluxes of $O^+$, $He^+$ and $H^+$ ions for CME storms (panels e1′–e2′–e3′) than CIR storms (panels e1–e2–e3). The correlation with AE-index is higher at $L > 3$ for $O^+$ ion fluxes with >10 keV for CME and CIR storms (e1–e1′), while a high CC is observed for $He^+$ and $H^+$ ion fluxes at lower $L$-values for >10 keV. For low-energy ions, a poor correlation is observed with the solar wind parameters and geomagnetic index.

### 3.3. Duration of Flux Enhancement

Figure 5 shows the average duration of persistence time ($\langle \Delta t \rangle$), which is defined as follows.

At a given $L$-value and energy, we calculated the duration for which $R_2 \geq 2$ in successive orbits, and referred to as $\Delta t$. Thus, $\langle \Delta t \rangle$ is calculated by taking the summation of $\Delta t$ and dividing it by the number of storms falling into the bin. The central black dashed vertical line divides the figure into two parts. Left half shows $\langle \Delta t \rangle$ as a function

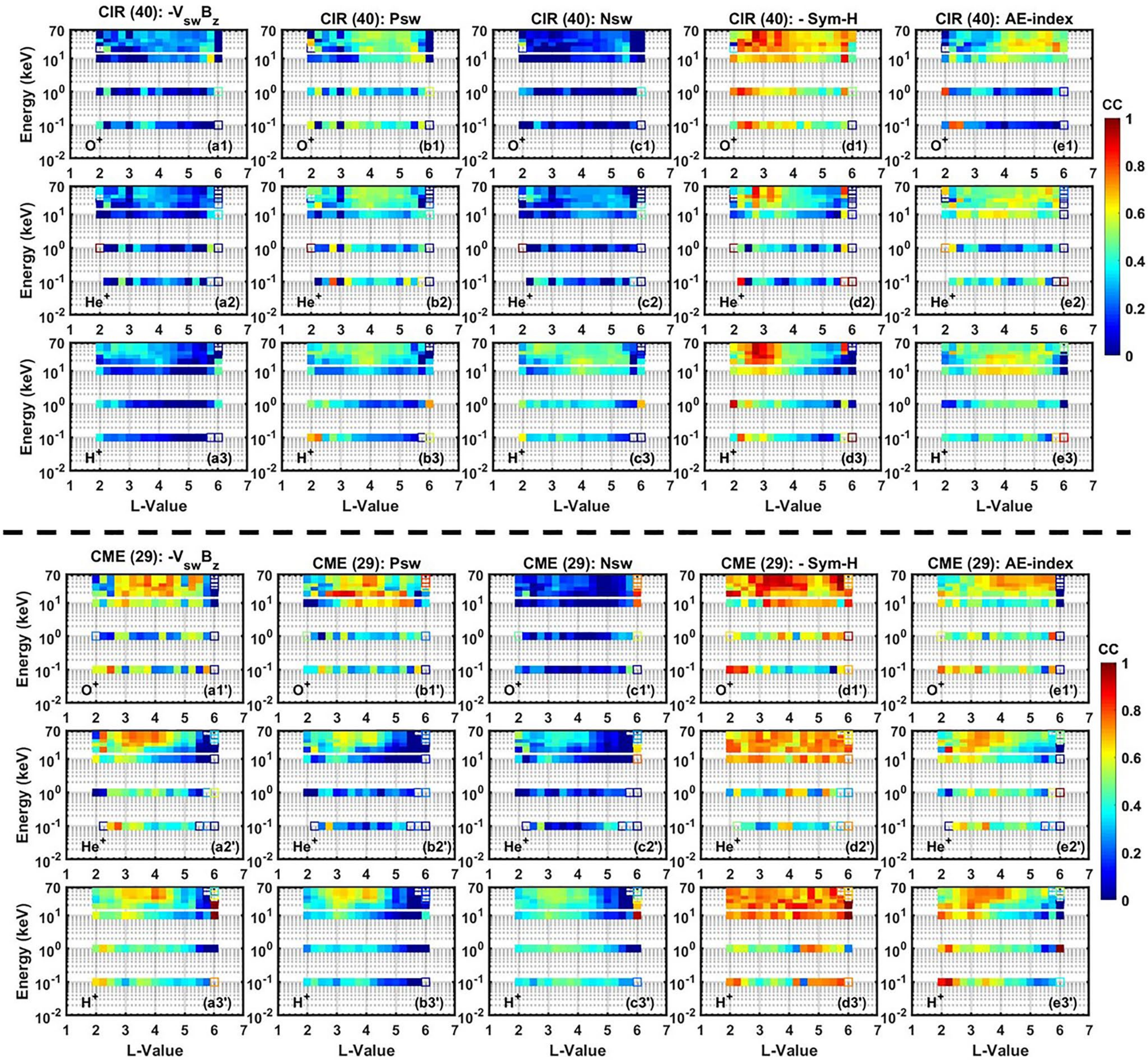


Figure 4. The correlation of various solar wind parameters and geomagnetic index with the fluxes of $O^+$, $He^+$, and $H^+$ ions as a function of *L*-value and energies is shown. Correlation coefficient (CC) is shown in colorbar. Black-dashed horizontal line separates the CIR-driven storms (upper half) from the CME-driven storms (lower half). The top-middle-bottom panels in each upper and lower half correspond to the CC of fluxes of $O^+$, $He^+$, and $H^+$ ions with different geophysical parameters. The open boxes represent the number of events being <3.

of both energies and *L*-value. The *y*-scale is adjusted such that it shows all the bands of selected energies. The distribution of the number of available cases is shown by the size of pixel (diamond). We separate $\langle \Delta t \rangle$ of $O^+$, $He^+$, and $H^+$ ion for CIR (a1–b1–c1) and CME storms (a2–b2–c2). Panels a1–a2 show that the $\langle \Delta t \rangle_{O^+}$ generally increase with the increasing *L*-value and energy, and that CIR storms have higher $\langle \Delta t \rangle_{O^+}$ than CME storms. Panels b1–b2 show that $\langle \Delta t \rangle_{He^+}$ increases with increase in *L*-value and energy. In panels c1–c2, we can see that $\langle \Delta t \rangle_{H^+}$ is relatively low at lower *L*-values for 0.1 keV to tens of keV and it is relatively high at $L > 4$ and energy >30 keV. $\langle \Delta t \rangle_{H^+}$ is higher for CIR storms than CME storms, but $\langle \Delta t \rangle_{H^+}$ is much lower than $\langle \Delta t \rangle_{O^+}$ for both the solar wind drivers. The results showing increasing tendency of $\langle \Delta t \rangle_{O^+}$ and $\langle \Delta t \rangle_{H^+}$ ions with *L*-value are well consistent with the study of A. Chen et al. (2021). A general tendency is found that considering each *L*-value and energy, $\langle \Delta t \rangle_{O^+} > \langle \Delta t \rangle_{He^+} > \langle \Delta t \rangle_{H^+}$ and that CIR storms show greater $\langle \Delta t \rangle$ than CME storms at a given *L*-value

 10.1029/2022JA030568

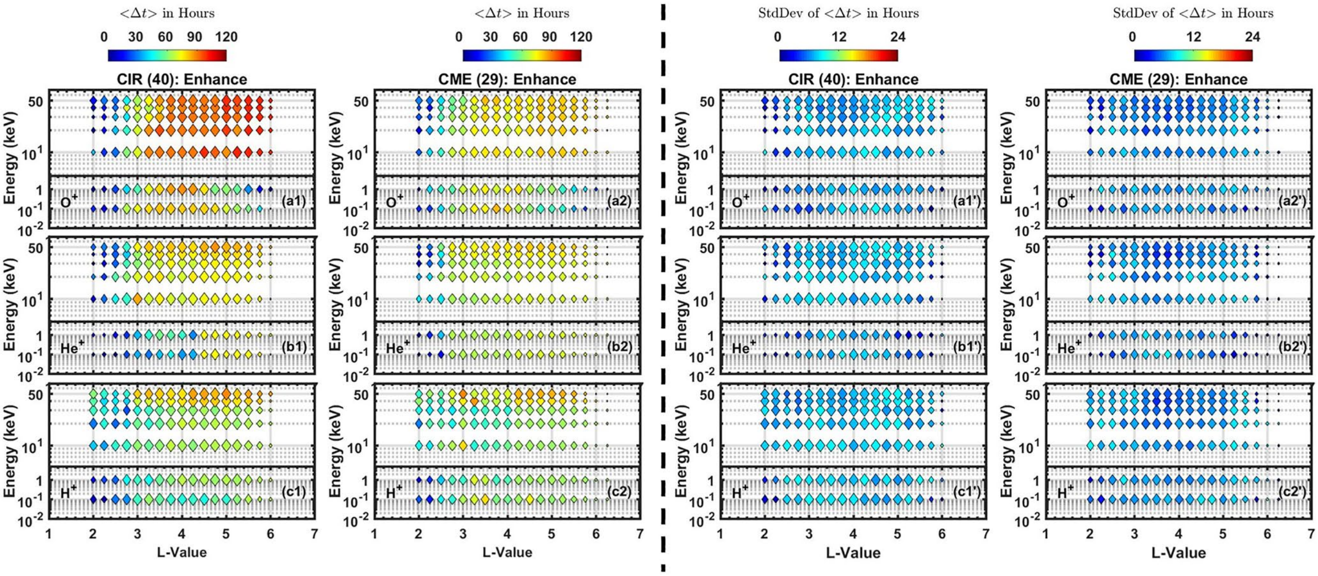


**Figure 5.** Central black dashed vertical line separates the figure into two. The left half shows the average duration of the persistence ($\langle \Delta t \rangle$) for $R_2 \geq 2$. Panels a1–b1–c1 show CIR storms while panels a2–b2–c2 show CME storms. The top-middle-bottom panels show the results of $O^+$, $He^+$, and $H^+$ ions, respectively. Number of available cases in every pixel of Energy and $L$-value is given by size of diamond. The $y$-scale is broken and adjusted such that it can show all the bands of selected energies. Right half of panel representation is same as the left half except for the colorbar that shows the standard deviation of $\langle \Delta t \rangle$.

and energy. To confirm the reliability of the results, we show the right half of Figure 5, which shows the standard deviation of $\langle \Delta t \rangle$. For every panel in the right half, we see that the standard deviation over a given pixel is <8 hr. Thus, it is reliable to consider $\langle \Delta t \rangle$ observations shown on the left half of Figure 5.

## 4. Discussion and Summary

We focused on 0.1–50 keV $O^+$, $He^+$, and $H^+$ ion variations in $2 \leq L \leq 6$ for 40 CIR and 29 CME-driven geomagnetic storms. The fluxes of all the measured ion species increased during the in-storm interval of the geomagnetic storm, but $O^+$ increased much more than $He^+$ and $H^+$. Storm-time variations of each ion species have also been investigated by many researchers (e.g., Daglis et al., 1999), but they do not distinguish driver of geomagnetic storms. A distinct characteristic difference is observed in the solar wind parameters between the CME and CIR-driven magnetic storms and their impacts on the Earth's magnetosphere. Hence, we statistically analyze the response of $O^+$, $He^+$, and $H^+$ ions in terms of $L$-value, energy, storm phase, and solar wind driver. Quantification of the ion fluxes is made by calculating the ratios of the fluxes taken during the in-storm interval to the pre-storm interval (i.e., $R_1$) and the ratios of the fluxes taken during the in-storm interval and the early recovery phase to the pre-storm interval (i.e., $R_2$).

At a given $(L, K)$ bin, a very similar (but not identical) percentage of events is observed for CIR and CME storms. For the CME storms $\bar{R}_1 \geq 2$ at $L \geq 2$ for all energies and species. This could be attributed to the nearly continuous plasma injection during the in-storm interval of the CME-driven storms. Ions with energy between ∼1 and ∼100 keV contribute most to the plasma pressure during storms (Smith & Hoffman, 1973). Recently, Mouikis et al. (2019) performed a statistical study using Van Allen Probes data to investigate the development and distribution of ring current plasma pressure for CME and CIR-driven storms. They presented the L-MLT distributions of partial pressure of $O^+$, $He^+$, and $H^+$ ions, but three classes of partial pressure are calculated for wide energy ranges of 0.1–55, 60–120, and 120–600 keV. Our analysis clarifies the details of $L$-shell and energy distributions of $O^+$, $He^+$, and $H^+$ ions fluxes at seven energy bins between 0.1 and 50 keV. Moreover, they found that the ring current pressure is mainly dominated by $< \sim 55$ keV $O^+$ ions during the CME-driven storms which are consistent with our results showing enhanced $O^+$ ion fluxes observed during the CME-driven storms.

The $\bar{R}_1(L, K)$ for $O^+$ ion flux is observed to be higher than $He^+$ and $H^+$ ions during the main phase of the CME storms. This is consistent with the observations at geosynchronous orbit, showing that the inferred $O^+$ density increases for CME storms in comparison with CIR storms (Denton et al., 2006). This is also relatable to Ogawa et al. (2019), which show a larger upward ionospheric flux outflow during CME-driven storms than those under CIR-driven storms.

Moreover we find that almost equivalent percentage of the events show $\bar{R}_1(L, K) \geq 2$ for <50 keV $O^+$ and $H^+$ ions for CME and CIR-driven geomagnetic storms. This agrees well with the studies by Keika, Kasahara, et al. (2018), where they examined the energy spectra of $O^+$ and $H^+$ ions during three-CME driven and three-CIR driven geomagnetic storms that occurred in the year 2017. They showed that the $O^+$ and $H^+$ ions with <50 keV contributes equally to the ring current energy density below $L = 5$, indicating the adiabatic transport of the low-energy ions from the plasma sheet by enhanced convection.

The $O^+$ and $H^+$ ions with 10–50 keV energies play an important role in the energy-dependent dynamics of Earth's inner magnetosphere. In Figure 3, we showed that the $O^+$ and $H^+$ ions with energies <50 keV are observed to enhance significantly during the main phase of the storm, with higher $\bar{R}_1(L, K)$ values for $O^+$ ions. This is consistent with the results by Zhao et al. (2015), where they studied the geomagnetic storm of March 29, 2013 and found that the low energy (<50 keV) ionospheric $O^+$ ions become a significant contributor to the ring current energy content during the main phase of the storm.

In addition, Denton et al. (2016) also showed that the $O^+$ ions with ~10 eV to >50 keV energies permeate $L < 6$ during June 2015 geomagnetic storm and become the dominant species during the storm main phase.

Yue et al. (2018) performed a statistical survey of equatorial plasma pressure distribution and showed that the ring current $O^+$ ion with $10 < E < 50$ keV is the dominant component of the plasma pressure during active times. Our results show that the dynamics of the proton fluxes is highly energy dependent. This is consistent with the studies by Gkioulidou et al. (2015) and Yi et al. (2021).

Gkioulidou et al. (2016) studied the $H^+$ ion pressure evolution using Van Allen Probes data and found that the convection process is mainly responsible or the transport and acceleration of <80 keV $H^+$ ion, while the radial diffusion is more dominant for (>100 keV) $H^+$ ion.

Keika, Seki, et al. (2018) examined the spatio-temporal variation of $O^+$ and $H^+$ energy density for March 17, 2015 geomagnetic storm and found that the ion energy ranges that contribute to the ring current evolve into three steps depending on the ion energies. During the first step, 20–80 keV ions dominate at $L$ ~3.5, which then starts to penetrate deeper to $L$ ~2.5 during the second step. As a last step, the energy ranges contributing to the energy density broadens close to the Sym-H minimum. Our results showed that the $H^+$ ion fluxes increased with increasing energies, consistent with the results reported by Yi et al. (2021), where they showed a global distribution of the proton energy spectra over 2013–2019 RBSPICE data set. They found that peculiar flux minima at low energy (50–100 keV) and flux maxima at higher energies (200–400 keV). However, charge exchange mechanism could not account for the loss of energy $H^+$ ions with 50–100 keV energies and hence the mechanism for the observed trend stands inconsistent with our results.

Menz et al. (2017) studied the ring current pressure buildup and the ion composition changes during the March 17, 2013 geomagnetic storm. They proposed that the enhanced convective transport from $L > 5.5$ to the inner magnetosphere could account for the enhanced $O^+$ ion pressure during the storm main phase at $L < 4$. However, the dominance of <45 keV $O^+$ ions over $H^+$ ions could be attributed to the low charge exchange rate of $O^+$ ions than $H^+$ ions below $L = 4$. This is consistent with our results showing $\langle \Delta t \rangle_{O^+} > \langle \Delta t \rangle_{H^+}$ (Figure 5).

The role of loss processes at specific values of the magnetic moment ($\mu$) for the $O^+$ ions is also addressed in the recent studies by Yue et al. (2021), where they showed the reduced fluxes of $O^+$ ions to form gap structures. They postulated that $O^+$ ion gaps resulting at specific $\mu$ values are the consequence of low drift speed leading to significant losses via charge exchange, Coulomb collision, or wave-particle interactions.

For better understanding, we characterize the relationship with various parameters on ion dynamics by correlating it with the fluxes of $O^+$, $He^+$, and $H^+$ ions as a function of $L$-value and energy, during the in-storm interval (Figure 4). A good correlation of $O^+$, $He^+$ and $H^+$ ion fluxes with $-V_{sw}B_z$ could be associated with the fact that southward driving of IMF is continuous in CME storms, while CIR storms tend to have fluctuation of southward component IMF for longer periods of time (Ebihara et al., 2002). This gives the strong correlation of ion fluxes with different solar wind parameters in CME storms. Moreover, during the main phase of the CME-driven storms, the solar wind velocity enhances that induces ULF waves in the Earth's inner magnetosphere that supports the growth of $O^+$ ions in the ring current region (Mitani et al., 2019; Tsurutani et al., 2006). Mitani et al. (2019)

showed that the ULF activity persists for a longer duration due to the high-speed solar wind stream during the recovery phase of CIR storms. This leads to a longer duration for the resonance and hence enhances the $O^+$ ion phase space density. Compression of the Earth's magnetosphere due to sudden increase in solar wind dynamic pressure leads to the outflow of ionospheric ions. For a particular event, Kronberg et al. (2012) showed that >274 keV $O^+$ ions show ~40 times flux enhancement with the change of about 1.25 nPa. Moreover, Elliott et al. (2001) and Cully et al. (2003) statistically showed that the escape of $O^+$ ions from the cusp region is well correlated with $P_{sw}$.

Figure 4 also provides new insight into the relationship between $N_{sw}$ and the ring current, which has been argued (O'Brien & McPherron, 2000; Smith et al., 1999; Thomsen et al., 1998). $N_{sw}$ may have two roles in the development of the ring current, (a) an energy driver that is responsible to the transport of the plasma sheet ions deep into the inner magnetosphere and (b) a mass driver that is responsible to the density of the seed ion population in the plasma sheet. Some energy coupling functions describing the rate of energy penetrating the magnetosphere depend on $N_{sw}$ (Temerin & Li, 2006; Wang et al., 2014). The simulation study performed by Lin et al. (2017) shows that the polar cap potential decreases with decreasing $N_{sw}$. This implies that the magnetospheric convection is supposed to increase with $N_{sw}$, and transport the plasma sheet ions deeper inward. If $N_{sw}$ acts as the energy driver of the ring current, CCs will be high independent of ionic species. This occurs when the Earth's magnetosphere undergoes a compression on the dayside which leads to an enhancement of the number density of all the ionic species irrespective of their masses. The ring current is also suggested to be intensified when the plasma sheet ions are high (Ebihara & Ejiri, 2000; Kozyra, Fok, et al., 1998). In that case, $N_{sw}$ acts as a mass driver of the ring current. If $N_{sw}$ acts as the mass driver of the ring current, CCs will be high for the solar wind-originated ions. Figure 4 clearly shows that CCs between $H^+$ and $N_{sw}$ are much larger than those between $He^+$ ($O^+$) and $N_{sw}$. This result is preferentially explained by the mass driver, rather than the transport driver since $O^+$ and $He^+$ are the ionospheric origin. Recently, Glocer et al. (2020) presented a simulation study to model the contribution of solar wind and ionospheric $O^+$ and $H^+$ to the ring current. They showed that during a geomagnetic storm, ionospheric protons can contribute as a dominant species to the ring current. Gloeckler and Hamilton (1987) estimated that 65% of the $H^+$ ion population is ionospheric origin during the storm main phase. Thus, $N_{sw}$ may also act as the transport driver, but its contribution would be small because of the fairly low CCs between $O^+$ ($He^+$) and $N_{sw}$.

Sym-H is more correlated with the ion fluxes, in particular, at 10–50 keV, likely suggesting that these ions are responsible for enhancing the storm-tine ring current, and changing the Sym-H index. This is consistent with the results by Gkioulidou et al. (2016), where they showed a high correlation between the Sym-H index and partial proton pressure (<80 keV). However, they do not investigate the dependence on ion species and solar wind parameters. We observed that the CCs between the AE index and the ion fluxes are also high, in particular, at 10–50 keV. It is likely that the enhancement of 10–50 keV ion fluxes is associated with the global reconfiguration of the magnetic field lines through depolarization or strong magnetic field line fluctuations (Gkioulidou et al., 2015; Keika et al., 2013). It is suggested that AE is high during the magnetic storms because the magnetic storms and substorms share the common solar wind parameters, namely, southward component of IMF and the fast solar wind (Kamide, 1992). To isolate the contribution from the substorms, further studies are necessary.

We show that $\langle \Delta t \rangle_{O^+} > \langle \Delta t \rangle_{He^+} > \langle \Delta t \rangle_{H^+}$ with CIR storms showing greater $\langle \Delta t \rangle$ than CME storms at a given $L$-value and energy. During the CIR-driven storms, the long-duration ULF waves are observed during the recovery phase; this leads to discrete injections and slow recovery even after the main phase of the geomagnetic storms (Mitani et al., 2019; Tsurutani et al., 2006). Three major loss mechanisms that have been suggested for the decay of the ring current are (a) charge exchange with the neutrals, (b) Coulomb collisions with thermal plasma in the plasmasphere, and (c) wave-particle interactions. The charge exchange with neutral atoms is thought to be a major loss process for ring current ions (e.g Kistler et al., 1989; Smith & Bewtra, 1978; Swisher & Frank, 1968). Our result shown in Figure 5 is partly consistent with the charge exchange loss: (a) $\langle \Delta t \rangle_{O^+} > \langle \Delta t \rangle_{H^+}$ for 0.1 to ~50 keV, (b) $\langle \Delta t \rangle_{O^+}$ and $\langle \Delta t \rangle_{H^+}$ are shown to increase with the increasing $L$-value. This could be attributed to the decrease in neutral number density with the increasing $L$. However, $\langle \Delta t \rangle_{He^+}$ is shorter than $\langle \Delta t \rangle_{O^+}$, which is inconsistent with expected charge exchange lifetime (cf. fig. 5 of Ebihara and Ejiri (2003)).

Our studies make a comprehensive analysis of the $O^+$, $He^+$, and $H^+$ ion dynamics in response to the varying solar wind conditions at different $L$-values and energies. The previous studies could not focus on the wide range of energies and $L$-values due to limited spatial coverage by the satellite and energy channels. Our new analysis reports the relationship of 0.1–50 keV ions to different solar wind and geomagnetic conditions. The major outcomes of our studies are summarized as:

1. We provide the information on the skewness of the distribution, in addition to the averaged values of fluxes for each ($L$, $K$) bin. Such analysis has not been addressed in previous studies.
2. Prolonged southward IMF leads to a continuous injection of charged particles in the Earth's inner magnetosphere. Thus, $-V_{sw}B_z$ shows the highest CC with $O^+$ ion fluxes for CME-driven storms than CIR storms at >1 keV energies.
3. $P_{sw}$ shows a good correlation (CC ~0.8) for $O^+$ ions during CME storms for >10 keV across $L$ ~2–5.5. This could be attributed to compression of the magnetosphere during enhanced $P_{sw}$ leading to the outflow of ionospheric ions. Beyond $L = 5.5$, the lower correlation could be attributed to the open drift trajectories of the ions that allows the access of fresh plasma sheet material (cf. Figure 2, Korth et al., 1999). Thus, $H^+$ and $He^+$ ions might persist always at $L > 5.5$ irrespective of the changes in $P_{sw}$.
4. The intensification of ring current is the major cause for strengthening of the geomagnetic storm. For CME and CIR-driven storms, $O^+$, $H^+$, and $He^+$ ion fluxes have higher CCs (0.6–0.9) with the intensity of the geomagnetic storms, measured by Sym-H and AE-index.
5. As $N_{sw}$ acts as a mass driver of the ring current, CC between $H^+$ ions and $N_{sw}$ is ~0.5, whereas CC between $O^+$ ions and $N_{sw}$ is poor.
6. $\langle \Delta t \rangle_i$ (where $i$ is $O^+$, $H^+$, or $He^+$) increases as $L$-value and energy increase. This is relatable with the decrease in number density and decrease in loss mechanisms with increasing $L$-value.
7. $\langle \Delta t \rangle_{O^+} > \langle \Delta t \rangle_{He^+} > \langle \Delta t \rangle_{H^+}$ for CIR storms which are greater than CME storms for ~<50 keV.

We highlight some of the main features that could be expected from the previous studies but also reveals some new relationships that are unexpected and not yet well-understood. The magnetic field lines undergo a significant distortion during the ring current formation due to the conservation of the first two adiabatic invariants (Ebihara et al., 2008). These newly discovered correlations show the need for future, more detailed, from the perspective of pitch angle distributions to further understand about the storm-time dynamics of ions in the inner magnetosphere. In addition, the variation of the ions with energy of the order of keV is known to depend on magnetic local time (MLT) during magnetic storms (Ebihara et al., 2002; Greenspan & Hamilton, 2000; Mouikis et al., 2019; Temporin & Ebihara, 2011). The MLT dependence is also an interesting topic to be studied in the future.

## Data Availability Statement

LANLGeoMag is downloadable at https://github.com/drsteve/LANLGeoMag.

**Acknowledgments**

The authors acknowledge the use of publicly available Van Allen Probes data of the Level 2 HOPE particle flux data obtained from the RBSP-ECT website (https://www.rbsp-ect.lanl.gov/science/DataDirectories.php/). The authors thank the Space Physics Data Facility at the NASA Goddard Space Flight Center for providing the OMNI data (https://cdaweb.gsfc.nasa.gov/index.html/). YE was supported by JSPS KAKENHI Grants 20H01960, and mission research at the Research Institute for Sustainable Humanosphere (RISH), Kyoto University.

## References

Allen, R. C., Livi, S. A., & Goldstein, J. (2016). Variations of oxygen charge state abundances in the global magnetosphere, as observed by Polar. *Journal of Geophysical Research: Space Physics*, *121*(2), 1091–1113. https://doi.org/10.1002/2015ja021765

Borovsky, J. E., & Denton, M. H. (2006). Differences between CME-driven storms and CIR-driven storms. *Journal of Geophysical Research*, *111*(A7), A07S08. https://doi.org/10.1029/2005ja011447

Borovsky, J. E., Thomsen, M. F., & Elphic, R. C. (1998). The driving of the plasma sheet by the solar wind. *Journal of Geophysical Research: Space Physics*, *103*(A8), 17617–17639. https://doi.org/10.1029/97ja02986

Boyle, C. B., Reiff, P. H., & Hairston, M. R. (1997). Empirical polar cap potentials. *Journal of Geophysical Research: Space Physics*, *102*(A1), 111–125. https://doi.org/10.1029/96ja01742

Burton, R. K., McPherron, R. L., & Russell, C. T. (1975). An empirical relationship between interplanetary conditions and Dst. *Journal of Geophysical Research*, *80*(31), 4204–4214. https://doi.org/10.1029/ja080i031p04204

Chen, A., Yue, C., Chen, H., Zong, Q., Fu, S., Wang, Y., & Ren, J. (2021). Ring current decay during geomagnetic storm recovery phase: Comparison between RBSP observations and theoretical modeling. *Journal of Geophysical Research: Space Physics*, *126*(1), e2020JA028500. https://doi.org/10.1029/2020ja028500

Chen, A. J. (1970). Penetration of low-energy protons deep into the magnetosphere. *Journal of Geophysical Research*, *75*(13), 2458–2467. https://doi.org/10.1029/ja075i013p02458

Chen, M. W., Roeder, J. L., Fennell, J. F., Lyons, L. R., & Schulz, M. (1998). Simulations of ring current proton pitch angle distributions. *Journal of Geophysical Research: Space Physics*, *103*(A1), 165–178. https://doi.org/10.1029/97ja02633

Chissom, B. S. (1970). Interpretation of the kurtosis statistic. *The American Statistician*, *24*(4), 19–22. https://doi.org/10.1080/00031305.1970.10477202

Clark-Carter, D. (2005). *Interquartile range*. John Wiley & Sons, Ltd. https://doi.org/10.1002/0470013192.bsa311

Cramer, W., Turner, N., Fok, M.-C., & Buzulukova, N. (2013). Effects of different geomagnetic storm drivers on the ring current: CRCM results. *Journal of Geophysical Research: Space Physics*, *118*(3), 1062–1073. https://doi.org/10.1002/jgra.50138

Cully, C., Donovan, E., Yau, A., & Opgenoorth, H. (2003). Supply of thermal ionospheric ions to the central plasma sheet. *Journal of Geophysical Research: Space Physics*, *108*(A2), 1092. https://doi.org/10.1029/2002ja009457

Daglis, I. A., Kamide, Y., Kasotakis, G., Mouikis, C., Wilken, B., Sarris, E., & Nakamura, R. (1998). Ion composition in the inner magnetosphere: Its importance and its potential role as a discriminator between storm-time substorms and non-storm substorms. *Paper presented at the Fourth International Conference on Substorms (ICS-4)* (pp. 767–772). https://doi.org/10.1007/978-94-011-4798-9_160

Daglis, I. A., Thorne, R. M., Baumjohann, W., & Orsini, S. (1999). The terrestrial ring current: Origin, formation, and decay. *Reviews of Geophysics*, *37*(4), 407–438. https://doi.org/10.1029/1999rg900009

Denton, M. H., Borovsky, J. E., Skoug, R. M., Thomsen, M. F., Lavraud, B., Henderson, M. G., et al. (2006). Geomagnetic storms driven by ICME- and CIR-dominated solar wind. *Journal of Geophysical Research*, *111*(A7), A07S07. https://doi.org/10.1029/2005ja011436

Denton, M. H., Reeves, G. D., Thomsen, M. F., Henderson, M. G., Friedel, R. H. W., Larsen, B., et al. (2016). The complex nature of storm-time ion dynamics: Transport and local acceleration. *Geophysical Research Letters*, *43*(19), 10059–10067. https://doi.org/10.1002/2016gl070878

Dessler, A. J., & Parker, E. N. (1959). Hydromagnetic theory of geomagnetic storms. *Journal of Geophysical Research*, *64*(12), 2239–2252. https://doi.org/10.1029/jz064i012p02239

Ebihara, Y., & Ejiri, M. (2000). Simulation study on fundamental properties of the storm-time ring current. *Journal of Geophysical Research: Space Physics*, *105*(A7), 15843–15859. https://doi.org/10.1029/1999ja900493

Ebihara, Y., & Ejiri, M. (2003). Numerical simulation of the ring current. *Space Science Reviews*, *105*(1), 377–452. https://doi.org/10.1023/a:1023905607888

Ebihara, Y., Ejiri, M., Nilsson, H., Sandahl, I., Milillo, A., Grande, M., et al. (2002). Statistical distribution of the storm-time proton ring current: POLAR measurements. *Geophysical Research Letters*, *29*(20), 30-1–30-4. https://doi.org/10.1029/2002gl015430

Ebihara, Y., Fok, M.-C., Blake, J., & Fennell, J. (2008). Magnetic coupling of the ring current and the radiation belt. *Journal of Geophysical Research: Space Physics*, *113*(A7), A07221. https://doi.org/10.1029/2008ja013267

Ebihara, Y., Kasahara, S., Seki, K., Miyoshi, Y., Fritz, T. A., Chen, J., et al. (2009). Simultaneous entry of oxygen ions originating from the Sun and Earth into the inner magnetosphere during magnetic storms. *Journal of Geophysical Research: Space Physics*, *114*(A5), A05219. https://doi.org/10.1029/2009ja014120

Elliott, H., Comfort, R. H., Craven, P. D., Chandler, M. O., & Moore, T. E. (2001). Solar wind influence on the oxygen content of ion outflow in the high-altitude polar cap during solar minimum conditions. *Journal of Geophysical Research: Space Physics*, *106*(A4), 6067–6084. https://doi.org/10.1029/2000ja003022

Fennell, J. F., Roeder, J. L., Grande, M., & Wilken, B. (1996). Oxygen charge state abundance in the inner magnetosphere. *AIP Conference Proceedings*, *383*, 145. https://doi.org/10.1063/1.51527

Finlay, C. C., Maus, S., Beggan, C. D., Hamoudi, M., Lowes, F. J., Olsen, N., & Thébault, E. (2010). Evaluation of candidate geomagnetic field models for IGRF-11. *Earth Planets and Space*, *62*(10), 787–804. https://doi.org/10.5047/eps.2010.11.005

Fok, M.-C., Kozyra, J., Nagy, A., & Cravens, T. (1991). Lifetime of ring current particles due to Coulomb collisions in the plasmasphere. *Journal of Geophysical Research: Space Physics*, *96*(A5), 7861–7867. https://doi.org/10.1029/90ja02620

Fok, M.-C., Kozyra, J., Nagy, A., Rasmussen, C., & Khazanov, G. (1993). Decay of equatorial ring current ions and associated aeronomical consequences. *Journal of Geophysical Research: Space Physics*, *98*(A11), 19381–19393. https://doi.org/10.1029/93ja01848

Fok, M.-C., Wolf, R. A., Spiro, R. W., & Moore, T. E. (2001). Comprehensive computational model of Earth's ring current. *Journal of Geophysical Research: Space Physics*, *106*(A5), 8417–8424. https://doi.org/10.1029/2000ja000235

Funsten, H. O., Skoug, R. M., Guthrie, A. A., MacDonald, E. A., Baldonado, J. R., Harper, R. W., et al. (2013). Helium, oxygen, proton, and electron (HOPE) mass spectrometer for the radiation belt storm probes mission. *Space Science Reviews*, *179*(1–4), 423–484. https://doi.org/10.1007/s11214-013-9968-7

Gkioulidou, M., Ohtani, S., Mitchell, D., Ukhorskiy, A., Reeves, G., Turner, D., et al. (2015). Spatial structure and temporal evolution of energetic particle injections in the inner magnetosphere during the 14 July 2013 substorm event. *Journal of Geophysical Research: Space Physics*, *120*(3), 1924–1938. https://doi.org/10.1002/2014ja020872

Gkioulidou, M., Ukhorskiy, A. Y., Mitchell, D. G., & Lanzerotti, L. J. (2016). Storm time dynamics of ring current protons: Implications for the long-term energy budget in the inner magnetosphere. *Geophysical Research Letters*, *43*(10), 4736–4744. https://doi.org/10.1002/2016gl068013

Glocer, A., Welling, D., Chappell, C. R., Toth, G., Fok, M.-C., Komar, C., et al. (2020). A case study on the origin of near-Earth plasma. *Journal of Geophysical Research: Space Physics*, *125*(11), e2020JA028205. https://doi.org/10.1029/2020ja028205

Gloeckler, G., & Hamilton, D. (1987). AMPTE ion composition results. *Physica Scripta*, *1987*(T18), 73. https://doi.org/10.1088/0031-8949/1987/t18/009

Gloeckler, G., Wilken, B., Stüdemann, W., Ipavich, F., Hovestadt, D., Hamilton, D., & Kremser, G. (1985). First composition measurement of the bulk of the storm-time ring current (1 to 300 keV/e) with AMPTE-CCE. *Geophysical Research Letters*, *12*(5), 325–328. https://doi.org/10.1029/gl012i005p00325

Gonzalez, W. D., Joselyn, J. A., Kamide, Y., Kroehl, H. W., Rostoker, G., Tsurutani, B. T., & Vasyliunas, V. M. (1994). What is a geomagnetic storm? *Journal of Geophysical Research*, *99*(A4), 5771. https://doi.org/10.1029/93ja02867

Gonzalez, W. D., Tsurutani, B. T., & de Gonzalez, A. L. C. (1999). Interplanetary origin of geomagnetic storms. *Space Science Reviews*, *88*(3/4), 529–562. https://doi.org/10.1023/a:1005160129098

Greenspan, M. E., & Hamilton, D. C. (2000). A test of the Dessler-Parker-Sckopke relation during magnetic storms. *Journal of Geophysical Research: Space Physics*, *105*(A3), 5419–5430. https://doi.org/10.1029/1999ja000284

Hamilton, D. C., Gloeckler, G., Ipavich, F., Stüdemann, W., Wilken, B., & Kremser, G. (1988). Ring current development during the great geomagnetic storm of February 1986. *Journal of Geophysical Research: Space Physics*, *93*(A12), 14343–14355. https://doi.org/10.1029/ja093ia12p14343

Jordanova, V. K., Farrugia, C. J., Janoo, L., Quinn, J. M., Torbert, R. B., Ogilvie, K. W., et al. (1998). October 1995 magnetic cloud and accompanying storm activity: Ring current evolution. *Journal of Geophysical Research: Space Physics*, *103*(A1), 79–92. https://doi.org/10.1029/97ja02367

Jordanova, V. K., Farrugia, C. J., Thorne, R., Khazanov, G., Reeves, G., & Thomsen, M. (2001). Modeling ring current proton precipitation by electromagnetic ion cyclotron waves during the May 14–16, 1997, storm. *Journal of Geophysical Research: Space Physics*, *106*(A1), 7–22. https://doi.org/10.1029/2000ja002008

Kamide, Y. (1992). Is substorm occurrence a necessary condition for a magnetic storm? *Journal of Geomagnetism and Geoelectricity*, *44*(2), 109–117. https://doi.org/10.5636/jgg.44.109

Katus, R. M., Liemohn, M. W., Ionides, E. L., Ilie, R., Welling, D., & Sarno-Smith, L. K. (2015). Statistical analysis of the geomagnetic response to different solar wind drivers and the dependence on storm intensity. *Journal of Geophysical Research: Space Physics*, *120*(1), 310–327. https://doi.org/10.1002/2014ja020712

Keika, K., Kasahara, S., Yokota, S., Hoshino, M., Seki, K., Nosé, M., et al. (2018). Ion energies dominating energy density in the inner magnetosphere: Spatial distributions and composition, observed by arase/MEP-i. *Geophysical Research Letters*, *45*(22), 12153–12162. https://doi.org/10.1029/2018gl080047

Keika, K., Kistler, L. M., & Brandt, P. C. (2013). Energization of $O^+$ ions in the Earth's inner magnetosphere and the effects on ring current buildup: A review of previous observations and possible mechanisms. *Journal of Geophysical Research: Space Physics*, *118*(7), 4441–4464. https://doi.org/10.1002/jgra.50371

Keika, K., Nosé, M., Ohtani, S., Takahashi, K., Christon, S. P., & McEntire, R. W. (2005). Outflow of energetic ions from the magnetosphere and its contribution to the decay of the storm time ring current. *Journal of Geophysical Research: Space Physics*, *110*(A9), A09210. https://doi.org/10.1029/2004ja010970

Keika, K., Seki, K., Nosé, M., Miyoshi, Y., Lanzerotti, L. J., Mitchell, D. G., et al. (2018). Three-step buildup of the 17 March 2015 storm ring current: Implication for the cause of the unexpected storm intensification. *Journal of Geophysical Research: Space Physics*, *123*(1), 414–428. https://doi.org/10.1002/2017ja024462

Kistler, L., Ipavich, F., Hamilton, D., Gloeckler, G., Wilken, B., Kremser, G., & Stüdemann, W. (1989). Energy spectra of the major ion species in the ring current during geomagnetic storms. *Journal of Geophysical Research: Space Physics*, *94*(A4), 3579–3599. https://doi.org/10.1029/ja094ia04p03579

Korth, H., Thomsen, M. F., Borovsky, J. E., & McComas, D. J. (1999). Plasma sheet access to geosynchronous orbit. *Journal of Geophysical Research: Space Physics*, *104*(A11), 25047–25061. https://doi.org/10.1029/1999ja900292

Koskinen, H. E. J., & Kilpua, E. K. J. (2022). *Physics of Earth's radiation belts*. Springer International Publishing. https://doi.org/10.1007/978-3-030-82167-8

Kozyra, J. U., Fok, M., Sanchez, E., Evans, D., Hamilton, D., & Nagy, A. (1998). The role of precipitation losses in producing the rapid early recovery phase of the great magnetic storm of february 1986. *Journal of Geophysical Research*, *103*(A4), 6801–6814. https://doi.org/10.1029/97ja03330

Kozyra, J. U., Jordanova, V. K., Borovsky, J. E., Thomsen, M. F., Knipp, D. J., Evans, D. S., et al. (1998). Effects of a high-density plasma sheet on ring current development during the November 2-6, 1993, magnetic storm. *Journal of Geophysical Research: Space Physics*, *103*(A11), 26285–26305. https://doi.org/10.1029/98ja01964

Kremser, G., Stüdemann, W., Wilken, B., Gloeckler, G., Hamilton, D. C., & Ipavich, F. M. (1987). Average spatial distributions of energetic $O^+$, $O^{2+}$, $O^{6+}$, and $C^{6+}$ ions in the magnetosphere observed by AMPTE CCE. *Journal of Geophysical Research*, *92*(A5), 4459. https://doi.org/10.1029/ja092ia05p04459

Krimigis, S. M., Gloeckler, G., McEntire, R. W., Potemra, T. A., Scarf, F. L., & Shelley, E. G. (1985). Magnetic storm of September 4, 1984: A synthesis of ring current spectra and energy densities measured with AMPTE/CCE. *Geophysical Research Letters*, *12*(5), 329–332. https://doi.org/10.1029/gl012i005p00329

Kronberg, E. A., Ashour-Abdalla, M., Dandouras, I., Delcourt, D. C., Grigorenko, E. E., Kistler, L. M., et al. (2014). Circulation of heavy ions and their dynamical effects in the magnetosphere: Recent observations and models. *Space Science Reviews*, *184*(1–4), 173–235. https://doi.org/10.1007/s11214-014-0104-0

Kronberg, E. A., Haaland, S. E., Daly, P. W., Grigorenko, E. E., Kistler, L. M., Fränz, M., & Dandouras, I. (2012). Oxygen and hydrogen ion abundance in the near-Earth magnetosphere: Statistical results on the response to the geomagnetic and solar wind activity conditions. *Journal of Geophysical Research: Space Physics*, *117*(A12), A12208. https://doi.org/10.1029/2012ja018071

Lee, L., Corrick, G., & Akasofu, S.-I. (1983). On the ring current energy injection rate. *Planetary and Space Science*, *31*(8), 901–911. https://doi.org/10.1016/0032-0633(83)90145-9

Lennartsson, O. W. (1995). Statistical investigation of IMF Bz effects on energetic (0.1- to 16-keV) magnetospheric $O^+$ ions. *Journal of Geophysical Research*, *100*(A12), 23621. https://doi.org/10.1029/95ja02859

Liemohn, M. W., & Katus, R. (2012). Is the storm time response of the inner magnetospheric hot ions universally similar or driver dependent? *Journal of Geophysical Research: Space Physics*, *117*(A9), A00L03. https://doi.org/10.1029/2011ja017389

Lin, D., Zhang, B., Scales, W. A., Wiltberger, M., Clauer, C. R., & Xu, Z. (2017). The role of solar wind density in cross polar cap potential saturation under northward interplanetary magnetic field. *Geophysical Research Letters*, *44*(23), 11729–11734. https://doi.org/10.1002/2017gl075275

Lundin, R., Lyons, L. R., & Pissarenko, N. (1980). Observations of the ring current composition at L <4. *Geophysical Research Letters*, *7*(6), 425–428. https://doi.org/10.1029/gl007i006p00425

Mauk, B. H., Fox, N. J., Kanekal, S. G., Kessel, R. L., Sibeck, D. G., & Ukhorskiy, A. (2012). Science objectives and rationale for the radiation belt storm probes mission. *Space Science Reviews*, *179*(1–4), 3–27. https://doi.org/10.1007/s11214-012-9908-y

Menz, A. M., Kistler, L. M., Mouikis, C. G., Spence, H. E., Skoug, R. M., Funsten, H. O., et al. (2017). The role of convection in the buildup of the ring current pressure during the 17 March 2013 storm. *Journal of Geophysical Research: Space Physics*, *122*(1), 475–492. https://doi.org/10.1002/2016ja023358

Mitani, K., Seki, K., Keika, K., Gkioulidou, M., Lanzerotti, L. J., Mitchell, D. G., et al. (2019). Statistical study of selective oxygen increase in high-energy ring current ions during magnetic storms. *Journal of Geophysical Research: Space Physics*, *124*(5), 3193–3209. https://doi.org/10.1029/2018ja026168

Moore, T., Chandler, M., Fok, M.-C., Giles, B., Delcourt, D., Horwitz, J., & Pollock, C. (2001). Ring currents and internal plasma sources. *Space Science Reviews*, *95*(1), 555–568. https://doi.org/10.1023/A:1005264907107

Moore, T., Peterson, W., Russell, C., Chandler, M., Collier, M., Collin, H., et al. (1999). Ionospheric mass ejection in response to a CME. *Geophysical Research Letters*, *26*(15), 2339–2342. https://doi.org/10.1029/1999gl900456

Mouikis, C. G., Bingham, S., Kistler, L. M., Farrugia, C. J., Spence, H. E., Reeves, G., et al. (2019). The storm-time ring current response to ICMEs and CIRs using Van Allen Probe observations. *Journal of Geophysical Research: Space Physics*, *124*(11), 9017–9039. https://doi.org/10.1029/2019ja026695

Nosé, M., McEntire, R., & Christon, S. (2005). Influence of solar wind on source of ring current plasma. *COSPAR Colloquia Series*, *16*, 48–53. https://doi.org/10.1016/s0964-2749(05)80009-5

Nosé, M., Ohtani, S., Takahashi, K., Lui, A., McEntire, R., Williams, D., et al. (2001). Ion composition of the near-Earth plasma sheet in storm and quiet intervals: Geotail/EPIC measurements. *Journal of Geophysical Research: Space Physics*, *106*(A5), 8391–8403. https://doi.org/10.1029/2000ja000376

Nose, M., Takahashi, K., Ohtani, S., Christon, S., & McEntire, R. (2005). Dynamics of ions of ionospheric origin during magnetic storms: Their acceleration mechanism and transport path to ring current. *Geophysical Monograph*, *155*, 61–71. https://doi.org/10.1029/155gm08

O'Brien, T. P., & McPherron, R. L. (2000). Evidence against an independent solar wind density driver of the terrestrial ring current. *Geophysical Research Letters*, *27*(23), 3797–3799. https://doi.org/10.1029/2000gl012125

Ogawa, Y., Seki, K., Keika, K., & Ebihara, Y. (2019). Characteristics of CME-and CIR-driven ion upflows in the polar ionosphere. *Journal of Geophysical Research: Space Physics*, *124*(5), 3637–3649. https://doi.org/10.1029/2018ja025870

Olson, W., & Pfitzer, K. (1979). *Magnetospheric magnetic field modeling (Tech. Rep.)*. McDonnell Douglas Astronautics Co. https://doi.org/10.21236/ada067597

Pandya, M., Bhaskara, V., Ebihara, Y., Kanekal, S. G., & Baker, D. N. (2019). Variation of radiation belt electron flux during CME- and CIR-driven geomagnetic storms: Van Allen Probes observations. *Journal of Geophysical Research: Space Physics*, *124*(8), 6524–6540. https://doi.org/10.1029/2019ja026771

Reeves, G. D., McAdams, K. L., Friedel, R. H. W., & O'Brien, T. P. (2003). Acceleration and loss of relativistic electrons during geomagnetic storms. *Geophysical Research Letters*, *30*(10), 1529. https://doi.org/10.1029/2002gl016513

Roeder, J., Fennell, J., Chen, M., Schulz, M., Grande, M., & Livi, S. (1996). CRRES observations of the composition of the ring-current ion populations. *Advances in Space Research*, *17*(10), 17–24. https://doi.org/10.1016/0273-1177(95)00689-c

Roederer, J. G. (1970). *Dynamics of geomagnetically trapped radiation*. Springer Berlin Heidelberg. https://doi.org/10.1007/978-3-642-49300-3

Siscoe, G. L. (2002). Hill model of transpolar potential saturation: Comparisons with MHD simulations. *Journal of Geophysical Research*, *107*(A6). https://doi.org/10.1029/2001ja000109

Smith, J., & Hoffman, R. (1973). Ring current particle distributions during the magnetic storms of December 16–18, 1971. *Journal of Geophysical Research*, *78*(22), 4731–4737. https://doi.org/10.1029/ja078i022p04731

Smith, J. P., Thomsen, M. F., Borovsky, J. E., & Collier, M. (1999). Solar wind density as a driver for the ring current in mild storms. *Geophysical Research Letters*, *26*(13), 1797–1800. https://doi.org/10.1029/1999gl900341

Smith, P. H., & Bewtra, N. (1978). Charge exchange lifetimes for ring current ions. *Space Science Reviews*, *22*(3), 301–318. https://doi.org/10.1007/bf00239804

Swisher, R., & Frank, L. (1968). Lifetimes for low-energy protons in the outer radiation zone. *Journal of Geophysical Research*, *73*(17), 5665–5672. https://doi.org/10.1029/ja073i017p05665

Takahashi, S., Iyemori, T., & Takeda, M. (1990). A simulation of the storm-time ring current. *Planetary and Space Science*, *38*(9), 1133–1141. https://doi.org/10.1016/0032-0633(90)90021-h

Temerin, M., & Li, X. (2006). Dst model for 1995–2002. *Journal of Geophysical Research*, *111*(A4), A04221. https://doi.org/10.1029/2005ja011257

Temporin, A., & Ebihara, Y. (2011). Energy-dependent evolution of ring current protons during magnetic storms. *Journal of Geophysical Research: Space Physics*, *116*(A10), A10201. https://doi.org/10.1029/2011ja016692

Terasawa, T., Fujimoto, M., Mukai, T., Shinohara, I., Saito, Y., Yamamoto, T., et al. (1997). Solar wind control of density and temperature in the near-Earth plasma sheet: WIND/GEOTAIL collaboration. *Geophysical Research Letters*, *24*(8), 935–938. https://doi.org/10.1029/96gl04018

Thomsen, M. F., Borovsky, J. E., McComas, D. J., & Collier, M. R. (1998). Variability of the ring current source population. *Geophysical Research Letters*, *25*(18), 3481–3484. https://doi.org/10.1029/98gl02633

Tsurutani, B. T., McPherron, R. L., Gonzalez, W. D., Lu, G., Gopalswamy, N., & Guarnieri, F. L. (2006). Magnetic storms caused by corotating solar wind streams. *Recurrent Magnetic Storms: Corotating Solar Wind Streams*, *167*, 1–17. https://doi.org/10.1029/167gm03

Turner, N. E., Cramer, W. D., Earles, S. K., & Emery, B. A. (2009). Geoefficiency and energy partitioning in CIR-driven and CME-driven storms. *Journal of Atmospheric and Solar-Terrestrial Physics*, *71*(10–11), 1023–1031. https://doi.org/10.1016/j.jastp.2009.02.005

Usanova, M., Mann, I., Kale, Z., Rae, I., Sydora, R., Sandanger, M., et al. (2010). Conjugate ground and multisatellite observations of compression-related EMIC Pc1 waves and associated proton precipitation. *Journal of Geophysical Research: Space Physics*, *115*(A7), A07208. https://doi.org/10.1029/2009ja014935

Walt, M., & Voss, H. D. (2001). Losses of ring current ions by strong pitch angle scattering. *Geophysical Research Letters*, *28*(20), 3839–3841. https://doi.org/10.1029/2001gl013425

Wang, C., Han, J. P., Li, H., Peng, Z., & Richardson, J. D. (2014). Solar wind-magnetosphere energy coupling function fitting: Results from a global MHD simulation. *Journal of Geophysical Research: Space Physics*, *119*(8), 6199–6212. https://doi.org/10.1002/2014ja019834

Weimer, D. R. (2001). An improved model of ionospheric electric potentials including substorm perturbations and application to the geospace environment modeling November 24, 1996, event. *Journal of Geophysical Research: Space Physics*, *106*(A1), 407–416. https://doi.org/10.1029/2000ja000604

Yi, J., Fu, S., Ni, B., Gu, X., Hua, M., Xiang, Z., et al. (2021). Global distribution of reversed energy spectra of ring current protons based on van allen probes observations. *Geophysical Research Letters*, *48*(4), e2020GL091559. https://doi.org/10.1029/2020gl091559

Yue, C., Bortnik, J., Li, W., Ma, Q., Gkioulidou, M., Reeves, G. D., et al. (2018). The composition of plasma inside geostationary orbit based on van allen probes observations. *Journal of Geophysical Research: Space Physics*, *123*(8), 6478–6493. https://doi.org/10.1029/2018ja025344

Yue, C., Zhou, X.-Z., Bortnik, J., Zong, Q.-G., Li, Y., Ren, J., et al. (2021). Sustained oxygen spectral gaps and their dynamic evolution in the inner magnetosphere. *Journal of Geophysical Research: Space Physics*, *126*(4), e2020JA029092. https://doi.org/10.1029/2020ja029092

Zhao, H., Li, X., Baker, D. N., Fennell, J. F., Blake, J. B., Larsen, B. A., et al. (2015). The evolution of ring current ion energy density and energy content during geomagnetic storms based on Van Allen Probes measurements. *Journal of Geophysical Research: Space Physics*, *120*(9), 7493–7511. https://doi.org/10.1002/2015ja021533

Zong, Q.-G., Wilken, B., Fu, S. Y., Fritz, T. A., Korth, A., Hasebe, N., et al. (2001). Ring current oxygen ions escaping into the magnetosheath. *Journal of Geophysical Research: Space Physics*, *106*(A11), 25541–25556. https://doi.org/10.1029/2000ja000127